Nonlinear Dyn
https://doi.org/10.1007/s11071-024-10341-3

RESEARCH

Initials-dependent dynamics and synchronization in a memristor coupled memristive map

Qianhan Zhao · Han Bao · Xi Zhang · Huagan Wu · Bocheng Bao

Received: 23 July 2024 / Accepted: 12 September 2024

Abstract Due to the unique nonlinearity with inner states, coupling memristors can make the subsystems to generate initials-dependent dynamical evolutions and synchronization behaviors in memristive networks, thus providing guidance for engineering applications. To this end, this paper designs a discrete model of the memristor-coupled memristive map composed of two identical memristive maps and a memristor coupler, and focuses on the initials-dependent dynamics and synchronizations. The coupling model exhibits a collection of spatial fixed points, whose stability depends on the initial states of the two subsystem memristors and the coupled memristor. On this basis, extreme multistability appears as symmetric coexisting attractors and dynamical distributions. The synchronization transitions and the phase synchronization with different kinds of phase errors are elaborated, which shows the synchronization effect of the coupling intensity and initial states. The results clarify that this coupling model can exhibit initials-dependent dynamics and synchronicity behaviors under the influence of three memristors. Afterwards, an FPGA-based hardware platform is used to verify the correctness of numerical simulations.

Q. Zhao · H. Bao · X. Zhang · H. Wu · B. Bao (✉)
School of Microelectronics and Control Engineering, Changzhou University, Changzhou 213159, China
e-mail: mervinbao@126.com

Keywords Memristive map · Spatial fixed point · Extreme multistability · Synchronization · FPGA platform

1 Introduction

Chaos theory, as a relatively nascent research field, is an in-depth study of a class of systems characterized by highly intricate and unpredictable properties [1, 2]. Chaotic systems exhibit a range of distinctive characteristics, including sensitivity to initial conditions, aperiodicity, and statistical regularities [3, 4], which makes them valuable in different practical applications such as time series forecasting [5], video encryption [6], secure communication [7], geolocation-based hardware encryptor [8], compressive ghost imaging [9]. Within chaotic systems, nonlinearity plays a crucial role in generating complex orbital structures and chaotic behaviors, such as scroll attractors [10], extreme multistability [11], and various patterns of coexisting attractors [12]. Among them, the memristor, as a special nonlinear element with internal states, has the ability to boost system memory and impact past states, making the evolution process more historically dependent and nonlinear [13]. These characteristics are crucial for enhancing the complexity and unpredictability, hence the recent progress of memristors in applications such as secure communication [14], deep learning [15], and edge computing [16].

Published online: 18 September 2024

Compared with traditional linear damping and inertial elements, memristors can bring new coupling effects and functional expansions in chaotic systems, nonlinear circuits, and neural network systems [17–19]. Since these formed memristive maps exhibit different physical expressions, they can be effectively applied to the energy calculation and the design of equivalent oscillators [20]. Memristive maps generate chaos and maintain low average energy in discrete systems, which can provide guidance for energy definition and reliability verification [21]. In chaotic systems, memristors can effectively replicate the nonlinear behaviors and enables the control of chaos complexity [22, 23]; in nonlinear circuits, memristors can be utilized to achieve complex dynamics and memory functions, thereby offering new avenues for circuit design and optimization [24, 25]; within neural networks, memristors can emulate the changes in membrane potential and synaptic transmission processes of neurons, and facilitate the learning of neural networks [26, 27]. Furthermore, memristors are versatile components that can be integrated into both continuous and discrete systems, which can enhance the adaptability for system modeling and control [28–30]. Recently, Xu et al. [31] designed an implementable Hodgkin-Huxley circuit with two N-type locally active memristors that can generate periodic and chaotic firing activities. Wang et al. [32] presented a heterogeneous memristive Hopfield neural network using different activation functions that show multi-scroll chaos, state jumps and multi-type coexisting attractors. Tamba et al. [33] investigated the dynamical analysis of a four-dimensional chaotic system with hidden extreme multistability based on a flux-controlled memristor and its application in image encryption. Therefore, memristor couplers have the potential to amplify the nonlinearity, which can result in increased complexity, so as to expand the application fields.

The above memristive coupling effects provide the basis for the occurrence of synchronization, which enables subsystems to work cooperatively in the coupled network. Synchronization refers to the maintenance of a specific phase relationship or state consistency over time between two or more systems [34], and holds considerable potential for practical applications across malicious attacks defense [35], color image restoration [36], and energy diversity [37]. Scholars explore how synchronization can be achieved in chaotic systems, with the goal of uncovering the mechanism and multimodal transition of synchronization [38]. Significant advancements have been achieved in investigating the dynamical behaviors of complex systems by memristor coupling [39, 40]. Meanwhile, the utilization of bidirectional coupling in constructing memristive coupled networks enables the realization of different collective dynamics and chaotic synchronization by manipulating network parameters and connection modes [41–43]. Taking FitzHugh-Nagumo and Rössler oscillators as examples, Namura et al. [44] presented a method for optimizing mutual coupling functions to achieve fast and global synchronization. Using Hamilton energy and synchronization factor, Zhang et al. [45] constructed a bionic memristor synapse-coupled bimRulkov neuron network and analyzed the line-boosted complete synchronization and plane-boosted parallel offset synchronization firings. Based on the extensible locally active memristor and two map-based neurons, Hu et al. [46] designed a memristor synapse-coupled neuron model and explored the initial-controlled generation and transition of synchronization with spiking/bursting firing behaviors. Evidently, memristor couplers can induce diverse dynamical behaviors and synchronizations in coupling networks.

However, there is limited exploration of memristor bidirectional coupling through discrete memristive maps, with existing studies focusing on bidirectional coupling neurons [47] and bidirectional coupling discrete maps [48]. This coupling mechanism offers a precise expression of the interactions within complex systems. Previous studies have shown that extreme multistability and rich synchronization behaviors are uncommon in bidirectionally coupled discrete maps. Thus, this study introduces a novel approach coupling two discrete memristive maps with a memristor coupler. Two sine-bounded memristive maps are considered the subsystems and a hyperbolic tangent memristor serves as the coupler. On one side, the coexisting attractors resulting from the interactions of the coupling and subsystem memristors exhibit symmetry in the memristive network with the appearance of extreme multistability. While the concept of extreme multistability has been extensively studied [49], the influence of the subsystems initial states on symmetry, has been relatively overlooked. On the other side, the adopted coupling form significantly reduces the dimensions required to achieve synchronization in the discrete domain, while the diversity of phase synchronization associated with the initial states

is analyzed in depth. Furthermore, the nonlinearity of the internal state leads to discrepancies between subsystems, which induce synchronization patterns transitions between complete, reverse, and phase synchronous behaviors that strongly depend on the initial states.

The rest of this article is arranged as follows. In Sect. 2, the mathematical model of a memristor-coupled memristive map is presented and its stability distribution of spatial fixed points is developed. In Sect. 3, the symmetric coexistence of attractors and dynamical distributions induced by the initial states of the coupled memristor and subsystem memristors are numerically simulated. In Sect. 4, the initials-dependent synchronization transitions and different kinds of phase synchronization are revealed. In Sect. 5, an FPGA hardware platform is created to experimentally validate the numerical results.

2 Memristor-coupled memristive map

This section presents the mathematical model of a memristor-coupled memristive map (MCMM), achieved by linking two identical sine-bounded memristive maps bidirectionally via a discrete memristor. Then, with the fixed point theory, the stability of MCMM is determined.

2.1 Model formulation

An effective way to comprehensively analyze dynamical evolutions and synchronization behaviors is to take the memristor as a coupler to synchronize two identical memristive systems [50]. Motivated by this scheme, this section presents a novel discrete model of the memristor coupled memristive map.

The two-dimensional (2-D) sine-bounded memristive map proposed in [51] owns a simple and effective implementation scheme and can generate complex dynamics, coexisting attractors with riddled attraction basins, and initial state-induced effects. This map is defined by the equation as

$$\begin{cases} x_{n+1} = \sin[ax_n/(q_n^2 - b)], \\ q_{n+1} = q_n + x_n. \end{cases} \tag{1}$$

where x_n and q_n are the input and the state variable of the memristor with reciprocal quadratic memristance, respectively, and a and b are two control parameters.

Discrete chaotic systems typically exhibit nonlinearity, complexity, and randomness. The incorporation of memristors with activation functions has the potential to amplify the system's nonlinearity, memory capability, and chaotic characteristics. Such memristors with activation functions can describe the coupling effects and promote the generation of synchronization phenomena. Recently, a discrete model of the memristor with hyperbolic tangent function memristance was designed in [52], which is described as

$$\begin{cases} i_n = M(\varphi_n)v_n = \tanh(\varphi_n)v_n, \\ \varphi_{n+1} = \varphi_n + v_n, \end{cases} \tag{2}$$

where v_n, i_n, and φ_n denote the sampled values of voltage v, current i, and state variable φ at the n-th iteration, respectively, and φ_{n+1} is the sampled value of state variable φ at the $(n+1)$-th iteration. Note that $M(\varphi_n)$ signifies the memristance based on the hyperbolic tangent function at the n-th iteration. Since the range of the hyperbolic tangent function is within $[-1, 1]$, it has boundedness above and below and can effectively simulate the physical boundary effect of the memristor. This makes it possible to control the range of the output, which is beneficial for the stability and robustness of the discrete memristive system.

Taking two 2-D sine-bounded memristive maps as subsystems, then a five-dimensional (5-D) memristor coupled memristive map is obtained by bidirectional coupling of the two subsystems through the memristor in (2). MCMM contains two memristive chaotic systems described by the state variables $x_1(n)$ and $x_2(n)$, respectively. The two subsystems influence each other through the difference $x_1(n) - x_2(n)$ which serves as the input of the memristor, while the output of the memristor feeds back into the subsystems. Thus, MCMM can be expressed as

$$\begin{cases} x_1(n+1) = \sin(\dfrac{ax_1(n)}{\varphi_1(n)^2 - b}) + k(x_1(n) - x_2(n))\tanh(\varphi_3(n)), \\ \varphi_1(n+1) = x_1(n) + \varphi_1(n), \\ x_2(n+1) = \sin(\dfrac{ax_2(n)}{\varphi_2(n)^2 - b}) - k(x_1(n) - x_2(n))\tanh(\varphi_3(n)), \\ \varphi_2(n+1) = x_2(n) + \varphi_2(n), \\ \varphi_3(n+1) = \varphi_3(n) + (x_1(n) - x_2(n)), \end{cases} \tag{3}$$

where $(x_1(n), \varphi_1(n), x_2(n), \varphi_2(n), \varphi_3(n))$ are the five state variables, and the parameter k represents the coupling intensity between the two subsystems. In (3), there are three memristors, two of which are the inherent memristors in subsystems with reciprocal quadratic memristance, and one is the coupled memristor, with their internal states designated as $\varphi_1(n)$, $\varphi_2(n)$ and $\varphi_3(n)$, respectively.

The coupled memristive connection is established between the state variables $x_1(n)$ and $x_2(n)$, which in turn generates a coupled signal $k\tanh(\varphi_3(n))(x_1(n) - x_2(n))$ under the influence of the error signal $x_1(n) - x_2(n)$. This signal plays a crucial role in regulating the synchronization behaviors of the coupled system. The coupled signal is primarily affected by the coupling intensity and the initial states, which makes MCMM prone to numerous initial-state-sensitive dynamics and synchronous behaviors.

2.2 Spatial fixed point set and stability

In the analysis of discrete maps, stability features are commonly assessed through fixed point theory which can help predict the chaotic properties and complex dynamics [53]. Assume that the fixed point of MCMM is $S = (X_1, \Psi_1, X_2, \Psi_2, \Psi_3)$, which can be solved by the following equations

$$\begin{cases} X_1 = \sin\left(\dfrac{aX_1}{\Psi_1^2 - b}\right) + k(X_1 - X_2)\tanh(\Psi_3), \\ \Psi_1 = X_1 + \Phi_1, \\ X_2 = \sin\left(\dfrac{aX_2}{\Psi_2^2 - b}\right) - k(X_1 - X_2)\tanh(\Psi_3), \\ \Psi_2 = X_2 + \Psi_2, \\ \Psi_3 = \Psi_3 + (X_1 - X_2). \end{cases} \tag{4}$$

According to the third formula of (4), it can be deduced that $X_1 = X_2$. By substituting the known condition into the previous formula, the fixed point is calculated as $S = (0, \delta_1, 0, \delta_2, \delta_3)$, where $\delta_1, \delta_2, \delta_3$ are three arbitrary constants representing the initial states of three memristors, namely $\varphi_1(n)$, $\varphi_2(n)$, and $\varphi_3(n)$. Obviously, MCMM has a set of spatial fixed points, which indicates that the resulting dynamics are tightly dependent on the memristor initial states, and may result in the appearance of extreme multistability.

The stability of a fixed point is determined by the eigenvalues of the Jacobian matrix at that point. The Jacobian matrix for the spatial fixed points is defined as

$$\mathbf{J}_S = \begin{bmatrix} \dfrac{a}{\delta_1^2 - b} + k\tanh(\delta_3) & 0 & -k\tanh(\delta_3) & 0 & 0 \\ 1 & 1 & 0 & 0 & 0 \\ -k\tanh(\delta_3) & 0 & \dfrac{a}{\delta_2^2 - b} + k\tanh(\delta_3) & 0 & 0 \\ 0 & 0 & 1 & 1 & 0 \\ 1 & 0 & -1 & 0 & 1 \end{bmatrix}. \tag{5}$$

Let $\varepsilon = k\tanh(\delta_3)$, $\mu = a/{\delta_1}^2 - b$, $\eta = a/{\delta_2}^2 - b$, where ε, μ, and η are three variables. Therefore, the eigenvalues of the spatial fixed points can be obtained through the *eig* function in MATLAB, which is expressed as

$$\begin{aligned} &\lambda_1 = 1,\ \lambda_2 = 1,\ \lambda_3 = 1, \\ &\lambda_4 = \varepsilon + \frac{\mu + \eta}{2} - \frac{\sqrt{(\mu - \eta)^2 + 4\varepsilon^2}}{2}, \\ &\lambda_5 = \varepsilon + \frac{\mu + \eta}{2} + \frac{\sqrt{(\mu - \eta)^2 + 4\varepsilon^2}}{2}. \end{aligned} \tag{6}$$

Clearly, λ_1, λ_2 and λ_3 in (6) are all critically stable because their values are equal to 1. Therefore, the stability of the spatial fixed points can be determined by examining the eigenvalues λ_4 and λ_5. The fixed point S is considered unstable if either $|\lambda_4|$ or $|\lambda_5|$ exceeds 1, whereas it is critically stable when both eigenvalues are within the range of -1 to 1.

The values of λ_4 and λ_5 are contingent upon the control parameters and the memristor initial states, thus the stability of MCMM is intricately linked to the control parameters (a, b, k) and initial states $(\delta_1, \delta_2, \delta_3)$. In short, the spatial fixed points can be stable or unstable, which may generate infinitely coexisting attractors with the effects of the initial states. To visually demonstrate the stability distribution of λ_4 and λ_5, the stability distribution on the initial state planes is drawn in Fig. 1. The red region signifies the unstable region, where any feature root exceeds 1; conversely, the black region signifies the stable region, where both feature roots are below 1.

When the two subsystems are inversely coupled, with a coupling coefficient of $k = -0.3$, and the model parameters $a = b = 2$ are consistent with those set in [51], the stability distribution in the δ_1-δ_2 and δ_1-δ_3 planes is depicted in Fig. 1a1, a2. Obviously, after bidirectional coupling of the memristor, the stability distribution of MCMM exhibits a distinct difference

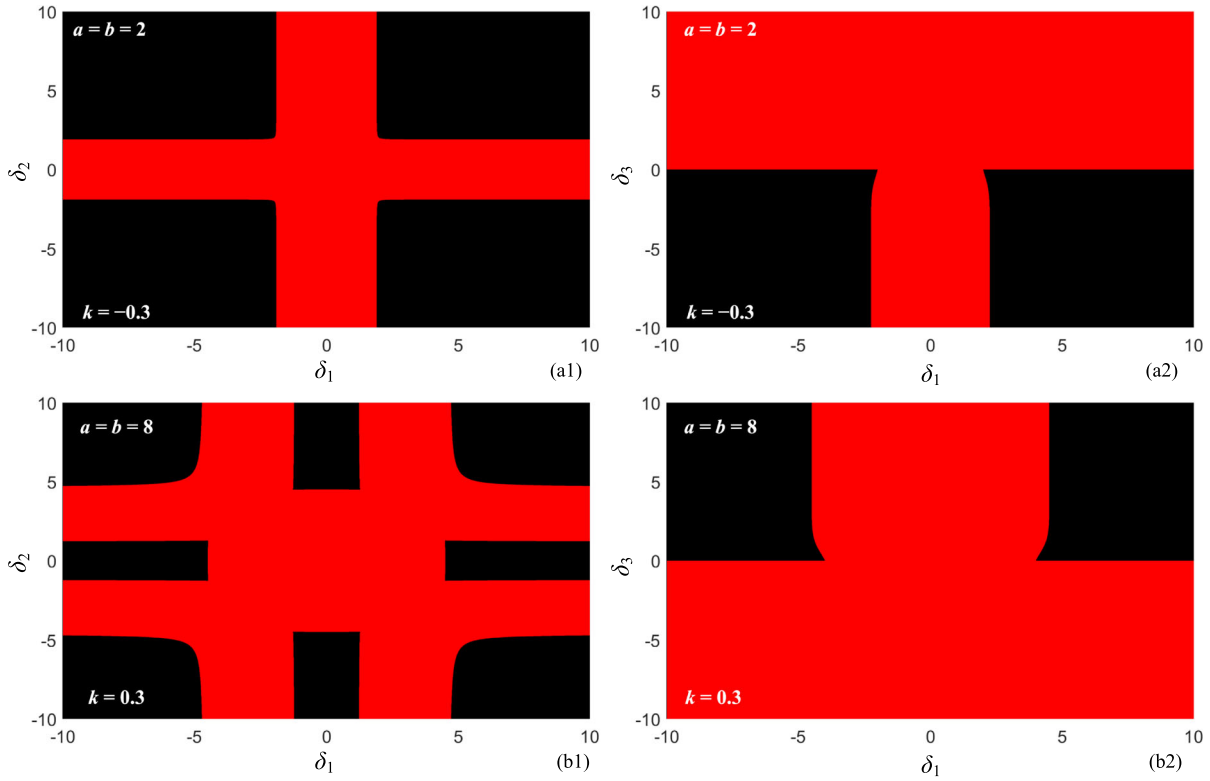

Fig. 1 Stability distributions of the spatial fixed point set in different initial state planes. **a** Fixing $k = -0.3$, $a = b = 2$, stability distribution plot in the δ_1–δ_2 plane and **b** the δ_1–δ_3 plane. **c** Fixing $k = 0.3$, $a = b = 8$, stability distribution plot in the δ_1–δ_2 plane and **d** the δ_1–δ_3 plane

from that of the original system, while still maintaining symmetry around the initial states. When k is assigned a positive value, the model parameter is set to $a = b = 8$, and the stability distribution in the initial state planes is illustrated in Fig. 1b1, b2. It can be seen that the stability distribution in the δ_1-δ_2 plane exhibits symmetry about the diagonal, while in the δ_1–δ_3 plane, it is symmetric solely about δ_1.

The results show that the memristive network possesses a set of spatial fixed points, which increases the degrees of freedom for the discrete map to capture the dynamic properties flexibly. Importantly, the stability is closely associated with both the control parameters and the initial states of three memristors, which may impact the dynamical evolutions of MCMM.

3 Initials-dependent complex dynamics

This section employs numerical methods to study extreme multistability, which are manifested as symmetric coexisting attractors induced by the initial states of three memristors and different dynamical distributions.

3.1 Bifurcation behaviors

It can be seen from the analysis in Sect. 2.2 that the fixed points and their stability are closely related to the initial states of three memristors. Therefore, the dynamical distributions in the initial state planes under the same parameter settings in Fig. 1 is plotted to further explore the effects of the initial states. The memristor initial states $(\varphi_1(0), \varphi_2(0), \varphi_3(0)) = (\delta_1, \delta_2, \delta_3)$ are taken as the variables, and the non-memristor initial states are fixed as $x_1(0) = 0.1, x_2(0) = 0$. Wolf's Jacobian algorithm is utilized to determine the Lyapunov exponent (LEs) of MCMM by tracking its evolution over an iteration length of 2×10^4. Combined with the calculation of the periodicities of the iterative sequences, the dynamical distribution in initial state planes can be obtained, as shown in Fig. 2.

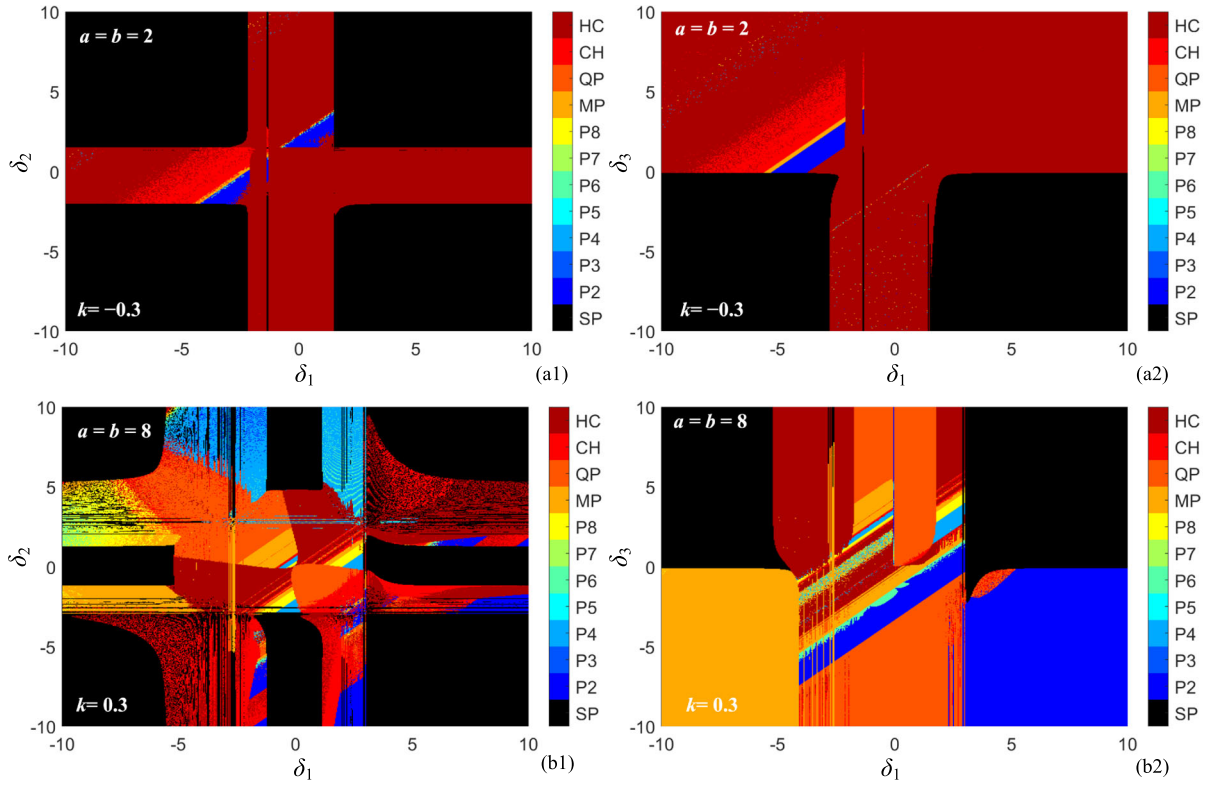

Fig. 2 Dynamical distributions in different initial state planes. **a** Fixing $k = -0.3$, $a = b = 2$, dynamical distribution plot in the δ_1–δ_2 plane and **b** the δ_1-δ_3 plane. **c** Fixing $k = 0.3$, $a = b = 8$, dynamical distribution plot in the δ_1–δ_2 plane and **d** the δ_1–δ_3 plane

Regions with different dynamical behaviors are classified by different color blocks. The brown, red, and orange blocks denote hyperchaos with two positive LEs (labeled HC), chaos with one positive LE (labeled CH), and quasi-period with one zero largest LE (labeled QP), respectively. The black and khaki blocks represent stable point with two negative LEs (labeled SP) and multi-period with two negative LEs (labeled MP with a cycle number of more than 8), respectively. The remaining color blocks range from period 2 to period 8 (labeled P2 to P8). Note that both period-doubling bifurcation paths and quasi-periodic bifurcation paths are present in Fig. 2, which represent the dynamical evolution from period 2 to period 4 to period 8 entries into chaos and quasi-period entry into chaos, respectively. Besides, chaotic crisis scenarios, which imply a direct transition of the dynamical region from hyperchaos to stable point behavior, are also observed.

In particular, when comparing the dynamical distributions in Fig. 2 with the stability distributions in Fig. 1, it is evident that they exhibit similar distributions. Specifically, the stable region corresponds to stable point behavior, while the unstable region corresponds to chaos/hyperchaos and other period behaviors except for stable point. This indicates that the stability of the coupled system at a given initial state may have a direct impact on its subsequent dynamics. In other words, the initial state effects will be reflected in the topological structures of the phase space. However, there are some slight inconsistencies between the two, which may be caused by the nonlinear effect of the eigenvalues and parameter disturbance.

Take the memristor initial state δ_3 as the bifurcation variable, and choose two sets of control parameters from Fig. 2. The dynamical evolution of $[-10,10]$ is depicted in Fig. 3 through the one-dimensional (1-D) hybrid bifurcation diagrams. In Fig. 3a, as δ_3 goes from negative to positive, MCMM undergoes a tangential bifurcation path at $\delta_3 = -0.2$. This is succeeded by a brief phase of periodic behaviors

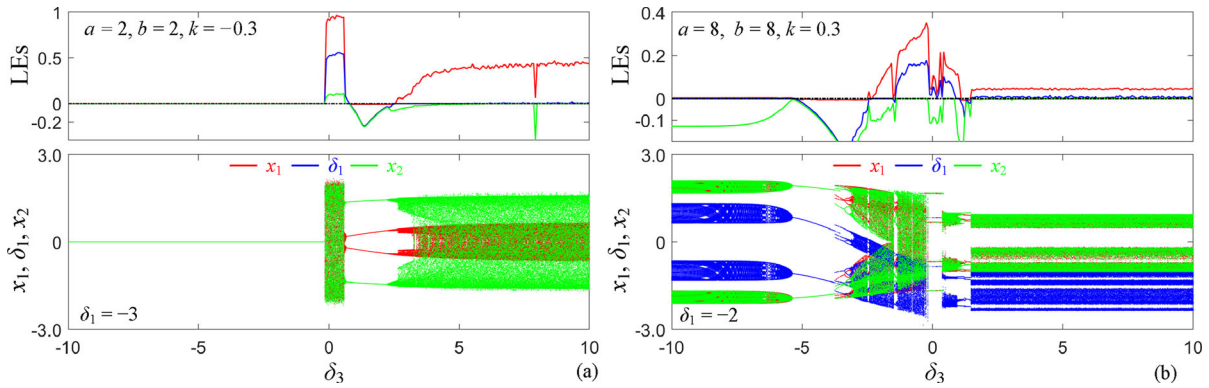

Fig. 3 Memristor initial state-relied hybrid bifurcation diagrams. **a** Fixing $k = -0.3$, $a = b = 2$, hybrid bifurcation diagrams with respect to δ_3. **b** Fixing $k = 0.3$, $a = b = 8$, hybrid bifurcation diagrams with respect to δ_3

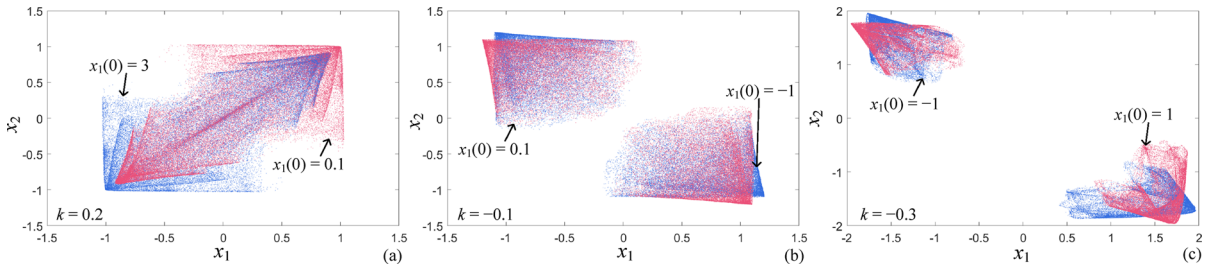

Fig. 4 Non-memristor initial state-relied attractors for different values of the coupling intensity k with $(a, b) = (-8, 1.3)$. **a** Symmetric attractors for varied $x_1(0)$ with $k = 0.2$. **b** Symmetric attractors for varied x_1 with $k = -0.1$. **c** Symmetric attractors for varied $x_1(0)$ with $k = -0.3$

before entering a broad range of chaos. As revealed in Fig. 3b, MCMM encounters a reverse quasi-periodic bifurcation path leading to hyperchaos at $\delta_3 = -5.3$ and a reverse period-doubling bifurcation path leading to robust chaos at $\delta_3 = 1.5$, along with some periodic windows. Consequently, the dynamical evolution of the memristor coupled system exhibits diverse behaviors under the control of the memristor initial states.

3.2 Symmetric coexisting attractors induced by three memristors

In a bidirectional coupled system, the coupling mode dictates the interaction between subsystems. If the coupling mode exhibits certain symmetry, the system may exhibit symmetric attractors under the control of different initial states [54]. For MCMM in (3), the control parameters are fixed as $(a, b) = (-8, 1.3)$, and the initial states are set to IS = $(x_1(0), \varphi_1(0), x_2(0), \varphi_2(0), \varphi_3(0)) = (0.1, 0, 0, 0, 3)$, with any initial state being a variable. For different values of the coupling intensity k, the symmetric coexisting attractors controlled by the initial state $x_1(0)$ are depicted in Fig. 4. The phase trajectories are plotted for iterations ranging from 1000 to 7000, excluding the transient states of the initial 1000 iterations.

It can be readily found from Fig. 4 that the symmetric coexisting attractors are diagonally distributed with different non-memristor initial states. These attractors are individually controlled by $x_1(0)$ and can undergo operations such as folding and rotation. This implies that the regulation of non-memristor initial states can exhibit symmetry and have effects on the topology of attractors.

If the control parameters are adjusted to $(a, b) = (-5.7, 0.6)$, the hyperchaotic attractors regulated by the initial states δ_1 and $x_1(0)$ at different values of the coupling intensity can be depicted in Fig. 5. The attractors in Fig. 5a, b can undergo symmetrical changes under the joint control of both memristor and non-memristor initial states, whereas the symmetric coexisting attractors in Fig. 5c, d are

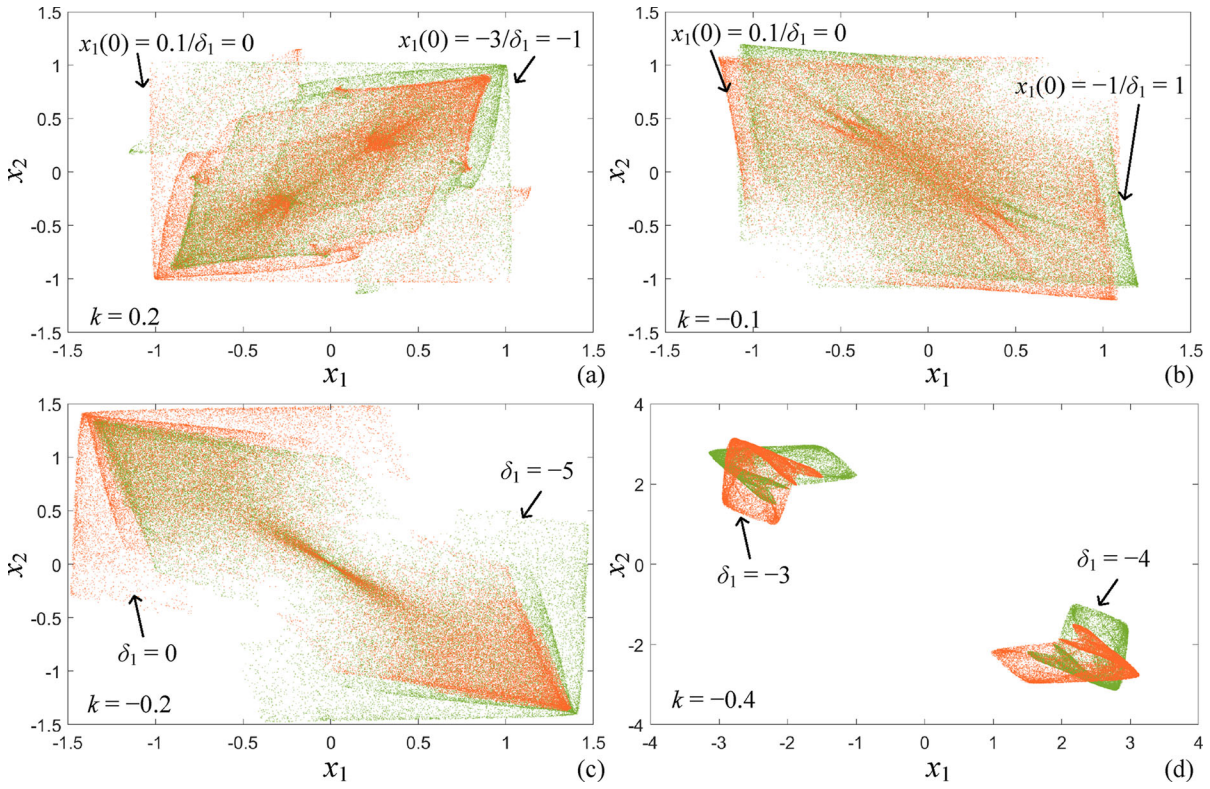

Fig. 5 Subsystem's memristor/non-memristor initial state-relied attractors for different values of the coupling intensity k with $(a, b) = (-5.7, 0.6)$. **a** Symmetric attractors for varied $x_1(0)/\delta_1$ with $k = 0.2$. **b** Symmetric attractors for varied $x_1(0)/\delta_1$ with $k = -0.1$. **c** Symmetric attractors for varied δ_1 with $k = -0.2$. **d** Symmetric attractors for varied δ_1 with $k = -0.4$

solely regulated by δ_1. This indicates that the coupled system can converge to a similar trajectory regardless of variations in initial states.

Similarly, when $(a, b) = (-3, -1)$, Fig. 6 shows the symmetric coexisting attractors independently controlled by the subsystem's memristor initial state δ_1, with other initial states fixed as $(x_1(0), x_2(0), \varphi_2(0), \varphi_3(0)) = (0.1, 0, 0, 3)$. The two-piece hyperchaotic attractors can be interchanged and folded independently along the diagonals. Particularly, the complete synchronization under the behavior of period 4 is illustrated in Fig. 6d, which indicates that the synchronization behavior can also show symmetry under the control of the initial states.

At the same time, we choose δ_3 as the varying parameter and further illustrate the impact of the coupled memristor initial state on the evolutions of dynamics. For fixed $(x_1(0), \varphi_1(0), x_2(0), \varphi_2(0)) = (0.1, 0, 0, 0)$, the symmetric coexisting attractors regulated by δ_3 under different control parameters are depicted in Fig. 7. As can be viewed, the attractors in Fig. 7a switches positions within the interior at $\delta_3 = 3$ and $\delta_3 = 8$, while the attractors in Fig. 7b are folded along negative diagonals at $\delta_3 = 0$ and 3, as well as at $\delta_3 = 7$ and 8, respectively. It demonstrates the coexistence of multi-symmetries in the phase plane.

These results indicate that the complex nonlinear behaviors of MCMM are tightly dependent on the initial states, which verify the effects of the initial states of three memristors. Through operations such as folding and rotating of the attractors, the system's diversified dynamical evolution path can be realized.

3.3 Extreme multistability

Based on the fixed point and stability analysis of MCMM in Sect. 2.2, it is evident that the initial states of the three memristors significantly impact the stability distribution. Thus, we utilize the local basins of attraction to further illustrate such effect of the

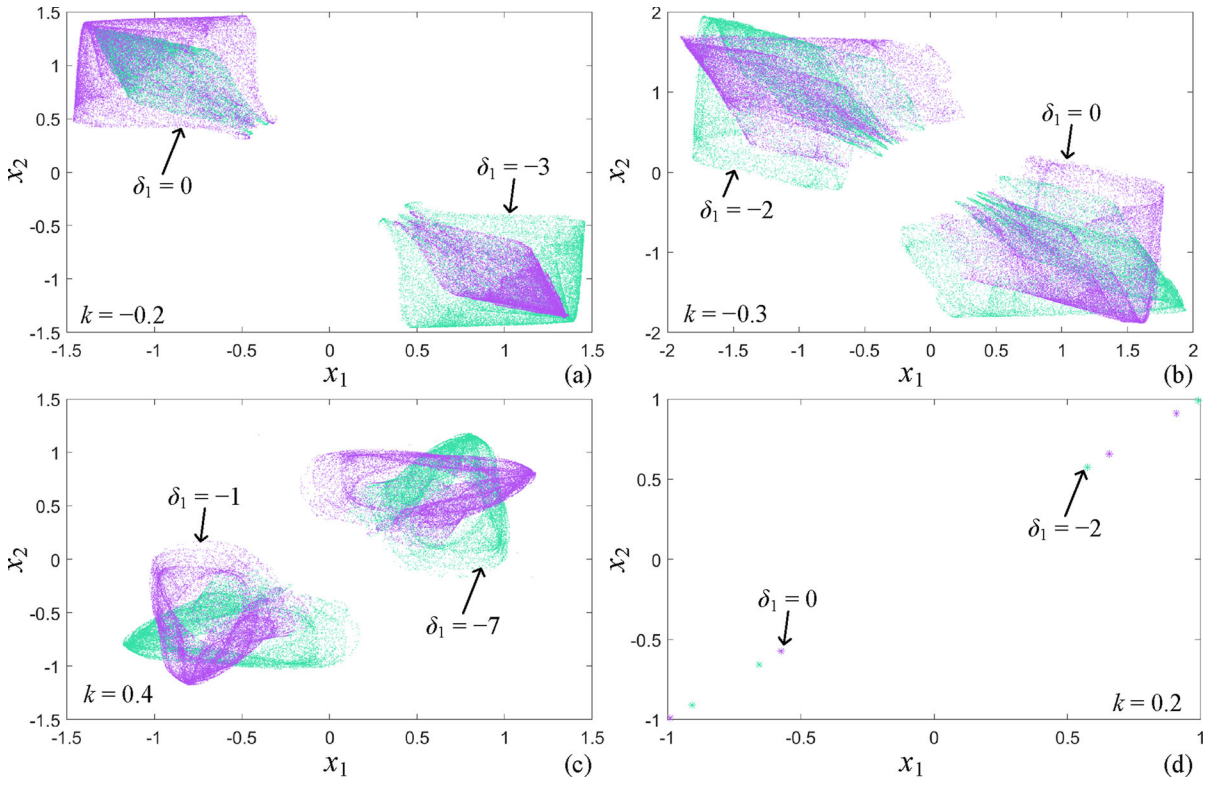

Fig. 6 Subsystem's memristor initial state-relied attractors for different values of coupling intensity with $(a, b) = (-3, -1)$. **a** Symmetric attractors for varied δ_1 with $k = -0.2$. **b** Symmetric attractors for varied δ_1 with $k = -0.3$. **c** Symmetric attractors for varied δ_1 with $k = 0.4$. **d** Symmetric attractors for varied δ_1 with $k = 0.2$

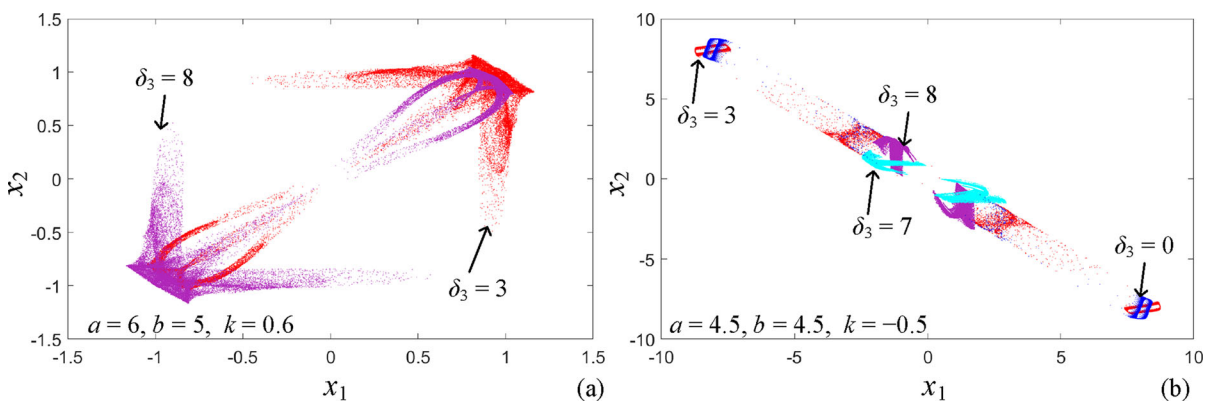

Fig. 7 Coupled memristor initial state-relied symmetric coexisting attractors for different values of the control parameters. **a** Symmetric attractors for varied δ_3 with $(a, b, k) = (6, 5, 0.6)$. **b** Symmetric attractors for varied δ_3 with $(a, b, k) = (4.5, 4.5, -0.5)$

initial states on dynamical distributions. Depending on the number of cycles of the iterative sequence and the calculation of the first two LEs with an iteration length of 2×10^4, different dynamical behaviors in the initial state planes are conveyed through different color blocks as in the arrangement of Fig. 2.

Following the symmetric coexisting attractors dependent on the initial states in Sect. 3.2, a specific set of control parameters in Fig. 6 is presented for plotting the basins of attraction in the $x_1(0)$–$x_2(0)$ plane, as depicted in Fig. 8. If $k = 0.2$ and 0.4 are chosen, it is evident that the initial state plane exhibits

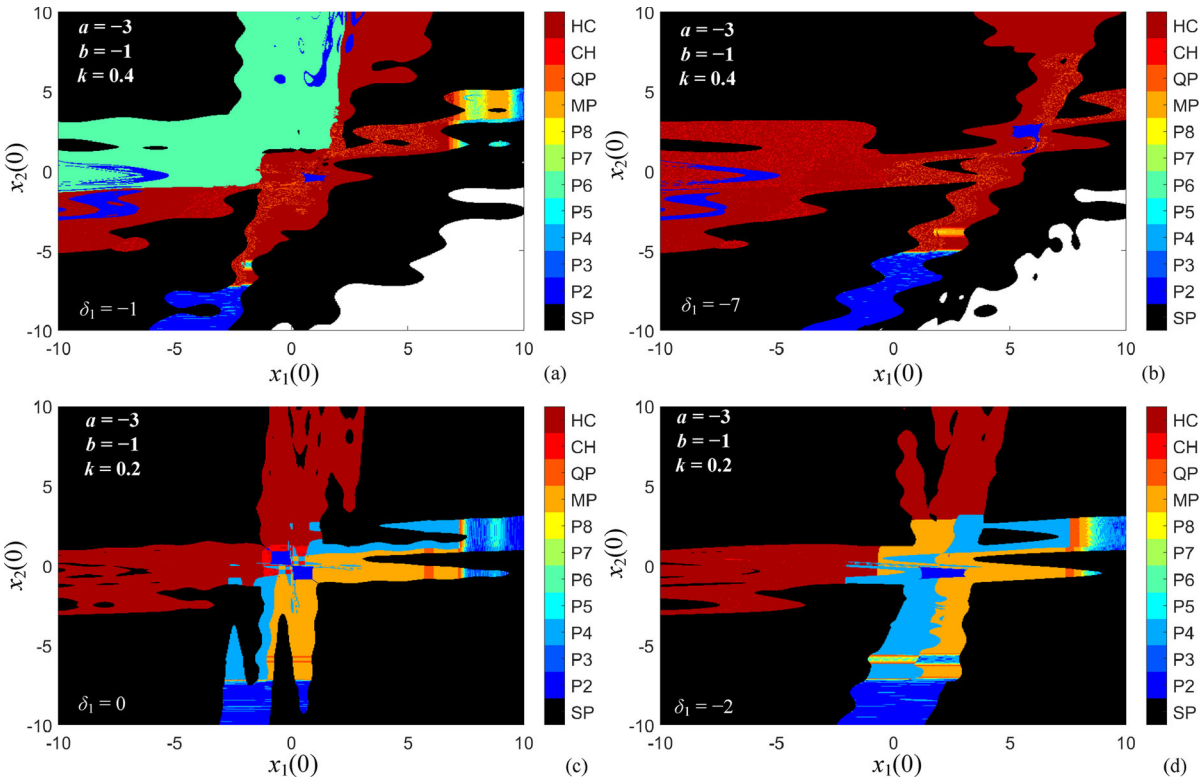

Fig. 8 When $(a, b) = (-3, -1)$, the 2D dynamical distributions in the $x_1(0)$-$x_2(0)$ plane with different values of δ_1. **a** Fixed $k = 0.4$, the dynamical distribution with $\delta_1 = -1$ and **b** $\delta_1 = -7$. **c** Fixed $k = 0.2$, the dynamical distribution with $\delta_1 = 0$ and **d** $\delta_1 = -2$

diverse states such as period and chaos, with different dynamical behaviors in the same region, which indicates the presence of extreme multistability in MCMM. In addition, affected by δ_1, the symmetry of the basins of attraction is shifted. When the disturbance is minimal like $\delta_1 = 0$ or -1, the basins of attraction are symmetric about the negative diagonal. As the disturbance increases gradually (e.g., with $\delta_1 = -2$ or -7), the basins of attraction shift towards the upper right corner, which leads to an asymmetrical distribution. Therefore, the distribution in the $x_1(0)$–$x_2(0)$ plane can exhibit complex symmetric dynamics that are extremely related to the coupling intensity and the initial states of the subsystem memristors.

Let the non-memristor initial state be assumed as $x_2(0) = 0$, while the control parameters are selected as those in Fig. 4, then the dynamical distributions in the δ_1–δ_2 initial state plane is illustrated in Fig. 9. It can be observed from Fig. 9a, c that the general shape is symmetrically distributed along the negative diagonal when the initial state disturbance is small, with only some asymmetry in different dynamical behaviors, which is caused by the changes of eigenvalues. Compared with Fig. 9a, the dynamical distribution in Fig. 9b shifts to the left with the increase of $x_1(0)$. Similarly, the dynamical distribution in Fig. 9d shifts towards the upper right corner as $|x_1(0)|$ increases. The results demonstrate that the variations in the coupling intensity and the non-memristor initial states significantly impact the dynamical distributions. In other words, MCMM is highly sensitive to the initial states which can result in extreme multistability and an infinite number of coexisting attractors in hyperchaotic regions.

4 Initials-dependent synchronization

In this section, we discuss the transitions of synchronous behaviors adjusted by the coupling intensity and the initial states, as well as analyze different kinds of phase synchronization generated by MCMM using phase difference plots.

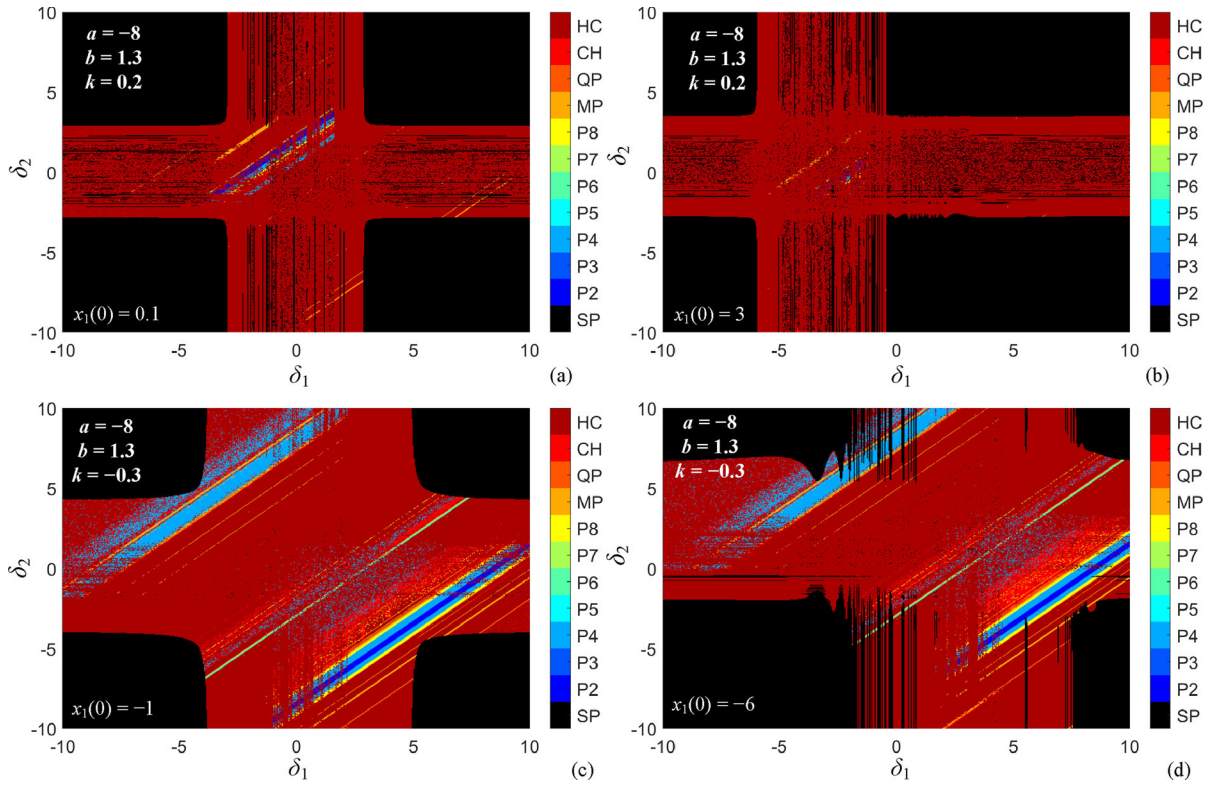

Fig. 9 When $(a, b) = (-8, 1.3)$, the 2D dynamical distributions in the δ_1–δ_2 plane with different values of $x_1(0)$. **a** Fixed $k = 0.2$, the dynamical distribution with $\delta_1 = -1$ and **b** $\delta_1 = -7$. **c** Fixed $k = -0.3$, the dynamical distribution with $\delta_1 = 0$ and **d** $\delta_1 = -2$

4.1 Synchronization transitions

Synchronization refers to the dynamical consistency or interrelation between two or more subsystems. Through the investigation of synchronization, we can uncover the interaction and regulatory mechanisms between subsystems, thereby affecting the behaviors of the coupled system [55]. Here, the normalized mean synchronization error (NMSE) is used to measure the synchronization characteristics between two subsystems. The approach involves normalizing the synchronization error for each iteration by dividing it with the overall average synchronization error and subsequently computing the mean of these standardized errors [56]. Therefore, the calculation formula for NMSE after the n-th iteration can be expressed as follows

$$\mathrm{NMSE} = \frac{1}{N}\sum_{n=1}^{N}\frac{\sqrt{(X_1(n)-X_2(n))^2+(Y_1(n)-Y_2(n))^2}}{\sqrt{X_1^2(n)+Y_1^2(n)+X_2^2(n)+Y_2^2(n)}}. \quad (7)$$

where N is the iteration sequence length which is set to 10^5 for accuracy and stability of calculation. As the NMSE tends towards zero, the two subsystems gradually approach the state of synchronization.

To explore the synchronization transitions between the two subsystems, the control parameters are defined as $(a, b) = (8, 3.6)$, with IS = $(x_1(0), \varphi_1(0), x_2(0), \varphi_2(0), \varphi_3(0)) = (0.1, 0, 0, 0, 3)$. Then the curve of NMSE between subsystems is depicted in Fig. 10a as a function of the variable k within the range of $[-0.5, 0.5]$. Three typical values are selected to draw the time sequences and phase diagrams in the x_1-x_2 plane, as shown in Fig. 10, with the red trajectory representing Subsystem 1 and the blue trajectory representing Subsystem 2. When $k = -0.4$, Fig. 10b shows complete synchronization of the chaotic state between the two subsystems, wherein the signals in dimensions x_1 and x_2 exhibit identical waveforms and phases, and are perfectly aligned in time. When $k = -0.02$,

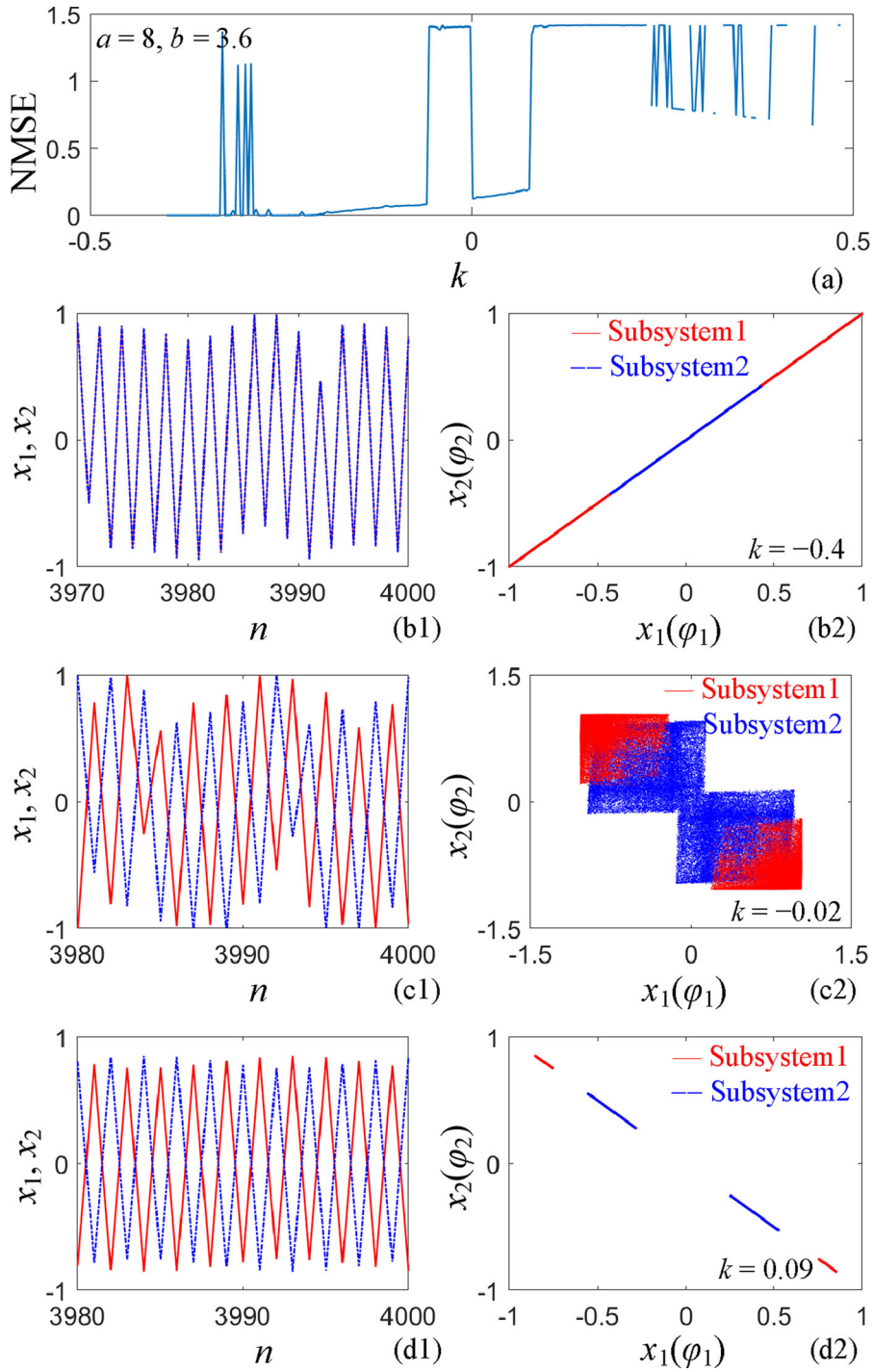

Fig. 10 When $(a, b) = (8, 3.6)$, NMSE curve respect to k and different synchronous behaviors. **a** NMSE curves respect to k. **b** Complete synchronization with $k = -0.4$. **c** Phase synchronization with $k = -0.02$. **d** Inverse synchronization with $k = 0.09$

Fig. 10c displays the phase synchronization, which indicates a constant phase difference between the signals x_1 and x_2 in the two subsystems. When $k = 0.09$, a chaotic state of inverse synchronization is presented in Fig. 10d. The crest of the signal x_1 corresponds to the trough of the signal x_2, that is, they are opposite in time, which describes the symmetric relationship between the two subsystems.

The synchronization properties of MCMM are also influenced by the control parameters and memristor

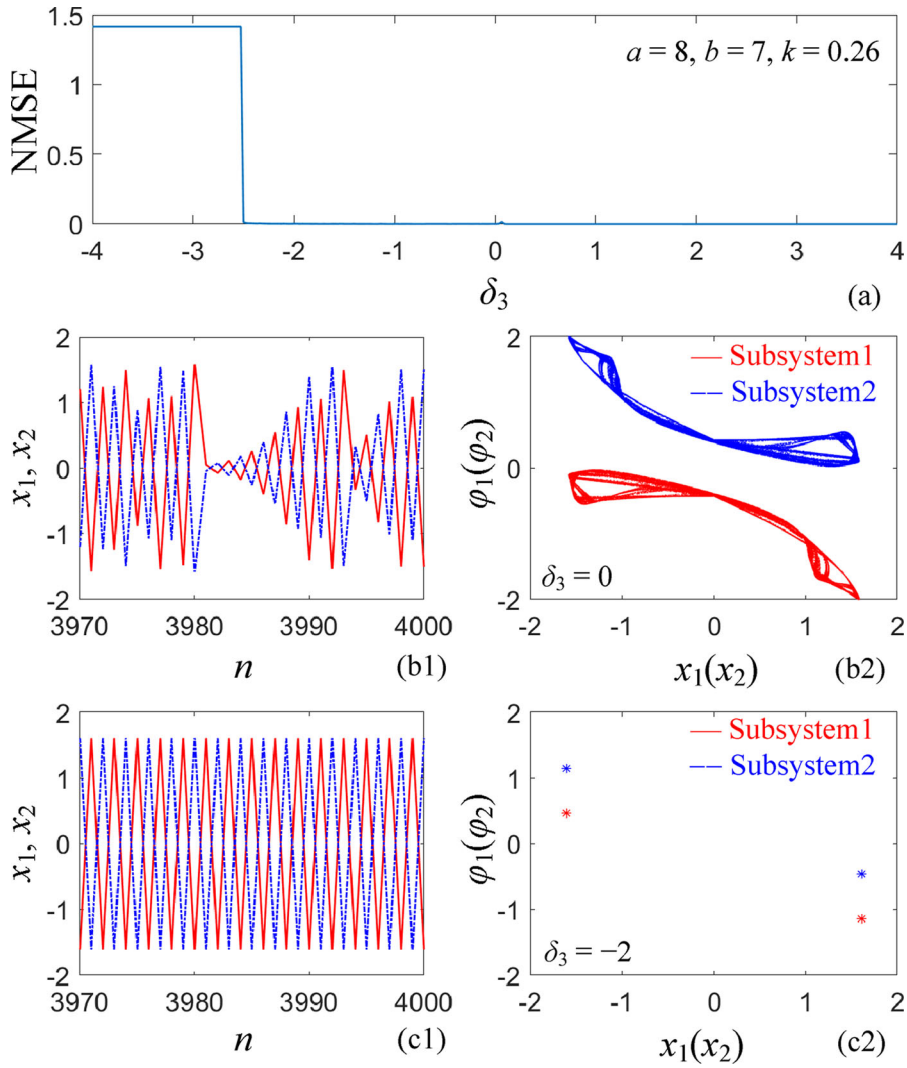

Fig. 11 When (a, b, k) = (8, 7, 0.26), NMSE curve respect to δ_3 and different synchronous behaviors. **a** NMSE curves respect to δ_3. **b** Inverse chaos synchronization with $\delta_3 = 0$. **c** Inverse period synchronization with $\delta_3 = -2$

initial states. Thus, to investigate the memristor initial-state-adjusted synchronous behaviors, the parameters are set as (a, b, k) = (8, 7, 0.26), and initial sates are IS = ($x_1(0)$, $\varphi_1(0)$, $x_2(0)$, $\varphi_2(0)$ = (0.1, 0, 0, 0). Similarly, the curve of NMSE between subsystems is depicted in Fig. 11a as a function of the variable δ_3 within the range of [− 4, 4]. As $\delta_3 = 0$, the inverse complete chaotic synchronization between subsystems is illustrated in Fig. 11b, where the iterations exhibit an inverse evolution and the phase projections in the x_1-φ_1 and x_2-φ_2 planes manifest as clear straight lines along the negative diagonal. For $\delta_3 = -2$, the coupled system shows the typical example of the inversely synchronized periodic behavior, as shown in Fig. 11c.

The findings indicate that the adjustment in the coupling intensity and the initial states can not only induce the transitions in synchronization behaviors, but also show the different dynamics within the same synchronization pattern.

4.2 Phase synchronization

Phase synchronization reflects the collective behavior within a chaotic system and refers to the synchronization mode in which two signals have the same or specific phase relationship [41]. The role of the coupled memristor instead of the external excitation allows the two subsystems to easily achieve phase

synchronization by positive coupling and negative coupling. Here, according to the definition in the literature [46], the formula for phase solution is

$$\theta(n) = 2\pi m + 2\pi \frac{n - n_m}{n_{m+1} - n_m}, (n_m < n < n_{m+1}), \quad (8)$$

where $2\pi m$ represents the basic phase value at the initial state, n_m represents the state of MCMM after the m-th iteration, while $n_{m+1} - n_m$ represents the delta or variation in the state between the $(m + 1)$-th and m-th iterations. Therefore, (8) implies that the phase value at n-th iteration is obtained by adding the initial phase $2\pi m$ to the newly corrected and adjusted phase value. This representation illustrates the phase transition and evolution in discrete maps.

The phase synchronization is identified by calculating the phase difference between the two subsystems, which is denoted as

$$|\Delta\theta(n)| = |\theta_1(n) - \theta_2(n)|, \quad (9)$$

here $\theta_1(n)$ and $\theta_2(n)$ are the phase values of the state variables $x_1(n)$ and $x_2(n)$, respectively. As the absolute value of the phase difference approaches a constant, it means that the two subsystems are synchronized in phase.

To demonstrate the coexistence of different kinds of phase synchronizations that depend on the coupling intensity and initial states, we present the time sequences and phase difference curves. The length of the time sequence is set within the range of [1200, 1300] to observe the relationship between the two sequences. However, a longer interval of [1000, 2000] is used to draw the phase difference curves for better visualization of the changes.

Followed by Fig. 10, the control parameters and initial states are set to $(a, b) = (8, 3.6)$ and $(x_1(0), \varphi_1(0), x_2(0), \varphi_2(0)) = (0.1, 0, 0, 0)$, then the phase synchronization associated with the coupling intensity k are plotted in Fig. 12. When $k = -0.4$, MCMM achieves complete synchronization in a chaotic state with $|\Delta\theta(n)| = 0$, thus realizing simultaneous phase synchronization. Similarly, when $k = 0.25$ and 0.33, the phase difference in Fig. 12b, c remains unchanged at 0, but the amplitude changes of sequences x_1 and x_2 are interchanged, which shows the diversity of phase synchronization dependent on coupling intensity.

By setting k to a fixed value of $k = -0.22$ and treating δ_3 as a variable, Fig. 13 illustrates the iterative sequences x_1, x_2 and the corresponding phase difference curves. For $\delta_3 = 1$, it is evident that the iteration sequences of the two subsystems do not exhibit complete coincidence, yet a negative phase difference $|\Delta\theta(n)| = -12.5$ is maintained, which indicates a lag relationship between subsystems. For $\delta_3 = 5$, the phase difference between the two subsystems is zero, and MCMM is in the state of complete chaotic synchronization. For $\delta_3 = 3$, Fig. 13c shows that at $n = 1260$ iterations, the phase difference undergoes a sudden change and stabilizes at a consistent value, which suggests the partial finite-time phase synchronization. The findings indicate that by controlling the initial state of the coupled memristor, the phase difference between subsystems can be limited to a certain constant range, while simultaneously inducing diverse phase synchronization behaviors.

To further demonstrate different phase synchronization behaviors adjusted by subsystems, Fig. 14 depicts the phase difference curves over iterations, with parameters and initial set as $(a, b, k) = (-6, 0.6, 0.2)$ and $\delta_3 = 0$. For $\delta_1 = -5$, the phase difference between subsystems presents incomplete phase synchronization under stepwise increase. In contrast, for $\delta_1 = 0$, the phase difference presents incomplete phase synchronization under stepwise decrease, with several phase difference pulses. The generation of this kind of phase synchronization may be related to the nonlinear effect and the fast-slow effect of the dynamical system. It is revealed that the phase difference fluctuation is highly sensitive to the initial states and coupling intensity, which leads to the diversity of phase synchronization behaviors.

To further emphasize the complexity of the constructed memristive network, we select a set of model parameters $(a, b, k) = (2, 1, -0.1)$ and evaluate the performance by some typical indicators for different initial states. These indicators include the first two LEs (LE_1, LE_2), spectral entropy (SE), permutation entropy (PE), and correlation dimension (CD). The evaluation results are enumerated in Table 1. As can be seen, MCMM exhibits hyperchaotic dynamics with the first two positive LEs, and have high performance indicators with SE up to 0.95, PE reaching 5.42, and CD exceeding 1.98. Obviously, modifying the memristor and non-memristor initial states will have an impact on the predictive ability and chaotic properties of the map, thereby affecting sensitivity to dynamics.

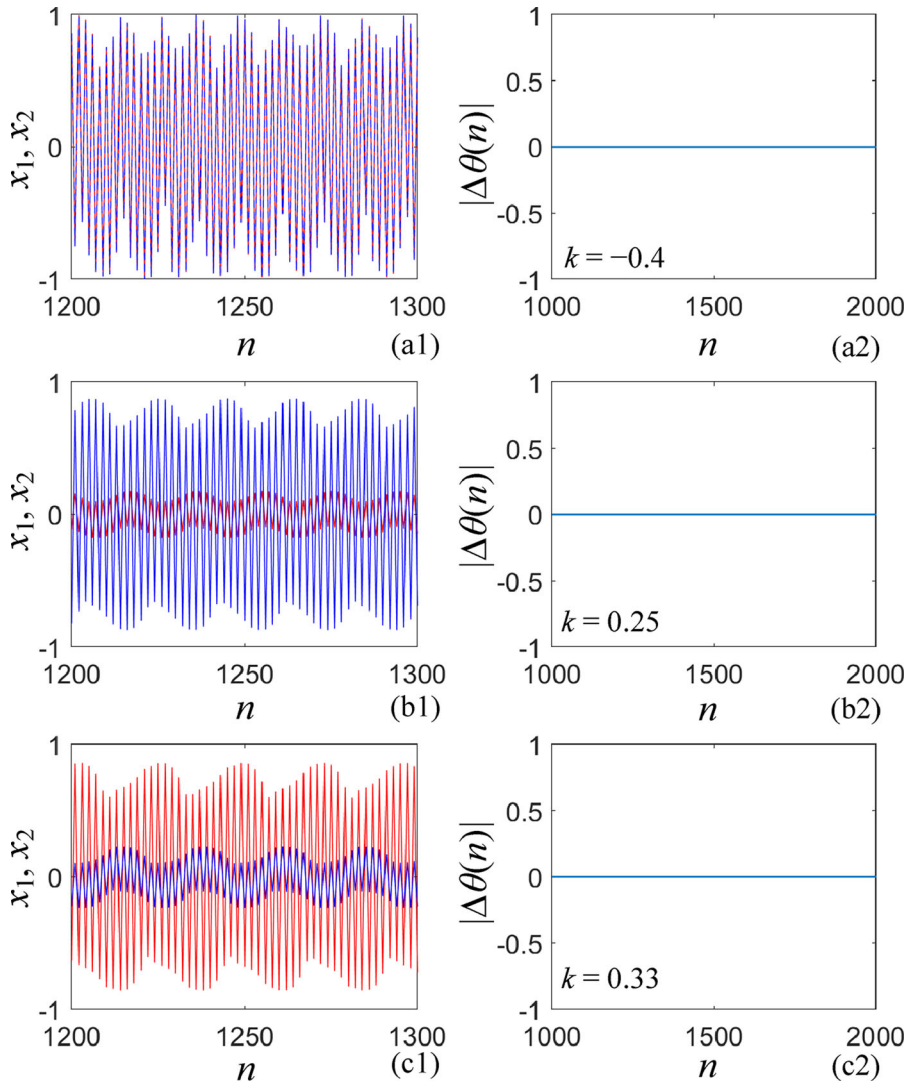

Fig. 12 When $(a, b) = (8, 3.6)$, times sequences and phase difference curves. **a** For $k = -0.4$, chaotic state in complete synchronization with $|\Delta\theta(n)| = 0$. **b** For $k = 0.25$, phase synchronization with $|\Delta\theta(n)| = 0$. **c** For $k = 0.33$, phase synchronization with $|\Delta\theta(n)| = 0$

The excellent performance under suitable parameters can ensure the reliability in practical applications.

5 FPGA hardware implementation

This section introduces an FPGA digital circuit implementation of MCMM, where symmetric coexisting attractors and synchronization transitions, dependent on the initial states and coupling intensity, are captured on the hardware platform. The programmable and parallel processing capability of the hardware platform provides an ideal solution for the digital implementation of discrete memristive maps.

To implement MCMM in (3) and validate its accuracy on FPGA, VHDL is employed for modeling and simulation based on the Vivado 2018.3 platform, followed by integrating onto Xilinx XC7Z100FFG900 development board. This process is mainly composed of designing modules, comprehensive realization, configuring the development board, as well as verification and debugging. In the module design section, 64-bit float-point number format is utilized to enable high-precision calculations. The floating-point IP cores such as addition, subtraction, multiplication, division, and sine support different floating-point number formats and operation modes, thereby accelerating complex mathematical operations and

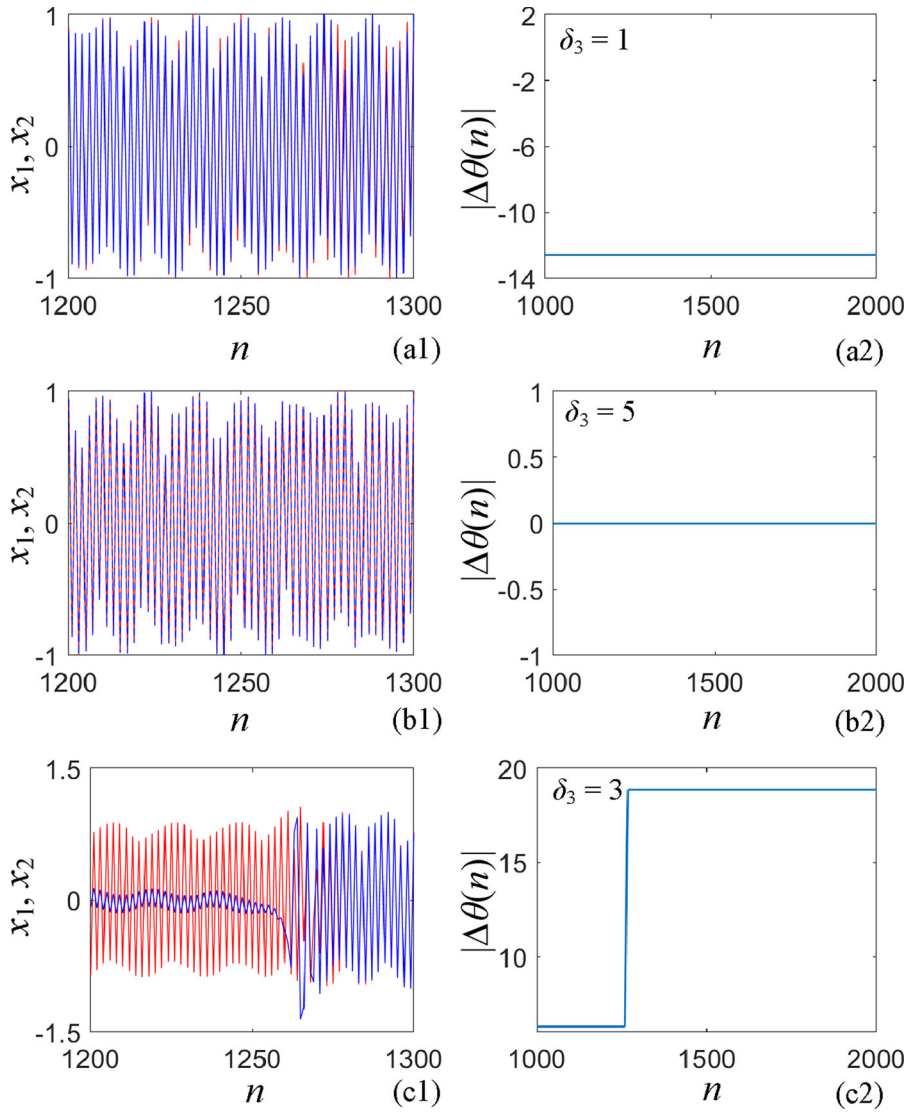

Fig. 13 When (a, b, k) = (8, 3.6, − 0.22), times sequences and phase difference curves respect to δ_3. **a** For δ_3 = 1, chaotic state in phase synchronization with $|\Delta\theta(n)|$= − 12.5. **b** For δ_3 = 5, chaotic state in complete and phase synchronization with $|\Delta\theta(n)|$= 0. **c** For δ_3 = 3, partial finite-time phase synchronization with $|\Delta\theta(n)|$= 6.2 when $n < 1260$ and $|\theta(n)|$= 18.8 when $n > 1260$

enhancing calculation speed and accuracy. In addition, the 14-bit AD9767 D/A module is utilized to facilitate the conversion of digital signals to analog signals for interfacing with external analog devices like the oscilloscope, which enables real-time signal monitoring. Then, a snapshot of the experimental environment and the captured attractor is shown in Fig. 15.

Particularly, the input range of the trigonometric IP core of the hardware platform is limited to (0, π). Hence, before the initial states enter the IP core, logic circuits are added for pre-processing. We process the input through the absolute value IP core to ensure it is non-negative and then normalize it. The comparator is used to perform cyclic subtraction to adjust the input and then calculate the cosine value, and the sine value is obtained through the trigonometric identity, which realizes the effective control of the input range.

The model parameters and initial states corresponding to the numerical simulations in Fig. 7 are preloaded into the platform, with (a, b, k) = (6, 5, 0.6) and (a, b, k) = (4.5, 4.5, − 0.5), respectively. For two different sets of δ_3, the attractors captured by the experimental time mode are shown in Fig. 16, which demonstrates the symmetric coexisting attractors controlled by the initial states consistent with the simulations. Similarly, the relevant parameters and initial state settings in Fig. 10 are selected as (a, b) = (8, 3.6) and IS = ($x_1(0)$, $\varphi_1(0)$, $x_2(0)$,

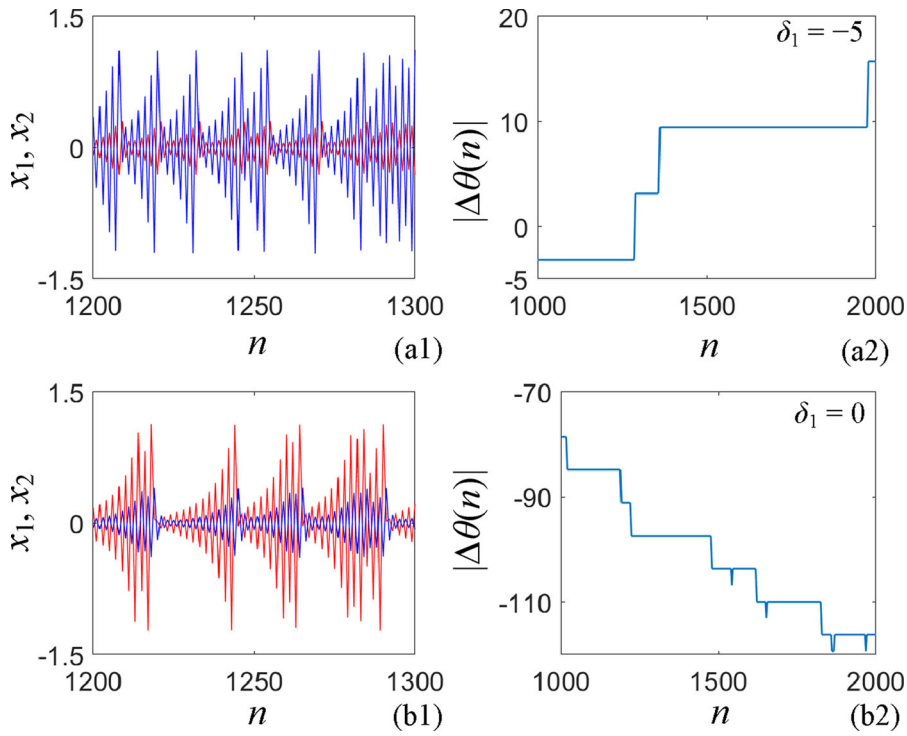

Fig. 14 When (a, b, k) = (− 6, 0.6, 0.2) and δ_3 = 0, times sequences and phase difference curves respect to δ_1. **a** For δ_1 = − 5, incomplete phase synchronization in stepwise increments. **b** For δ_1 = 0, incomplete phase synchronization in stepwise decrements

Table 1 Performance test results with (a, b, k) = (2, 1, − 0.1) for different initial states

δ_1, δ_3	LE_1, LE_2	SE	PE	CD
0, 3	1.2076, 0.5099	0.9552	5.1596	1.9819
− 2, 3	1.3332, 0.9980	0.8860	5.4205	2.0085
0, 0	1.2076, 0.5099	0.9559	5.0931	1.9853

$\varphi_2(0))$ = (0.1, 0, 0, 0), and the random hyperchaotic/chaotic sequences and attractors are captured experimentally in Fig. 17 under different values of the coupling intensity. It can be seen that the hardware experiment results of synchronization are in good agreement with the simulation contents, which verifies that the FPGA digital circuit can realize the initials-dependent dynamics and synchronization generated by MCMM.

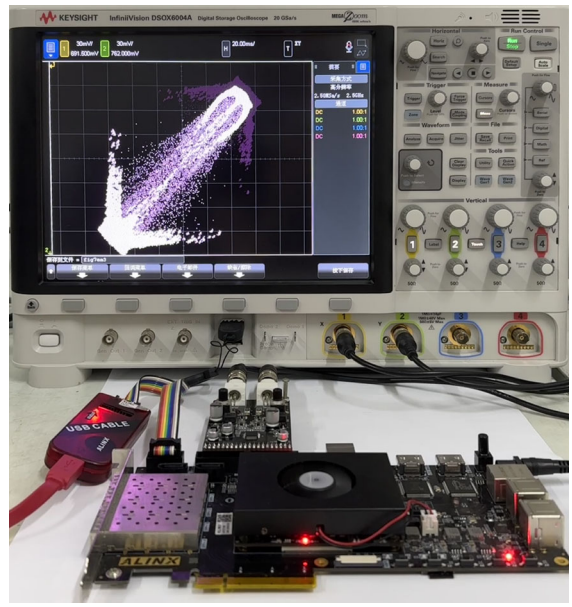

Fig. 15 A snapshot of the experimental environment and the captured symmetric attractor

6 Conclusion

In this paper, the initials-dependent symmetric coexisting attractors with extreme multistability were investigated and the synchronization transitions were realized in lower dimensions in comparison with continuous systems [56]. The memristor-coupled memristive map combined two sine-bounded memristive maps with the hyperbolic tangent memristor

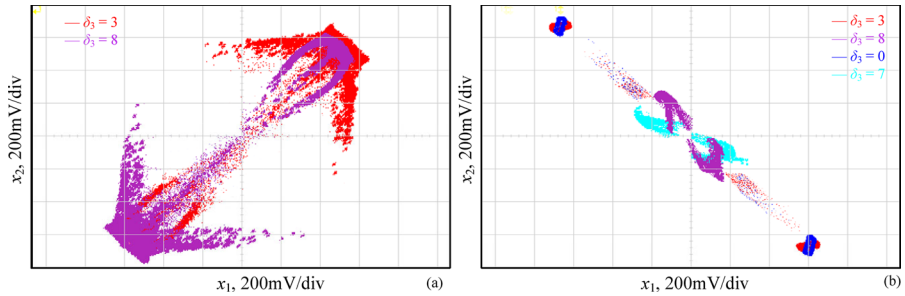

Fig. 16 The experimental memristor initial state-relied attractors for different values of control parameters. **a** Symmetric coexisting attractors for varied δ_3 with $(a, b, k) = (6, 5, 0.6)$. **b** Symmetric coexisting attractors for varied δ_3 with $(a, b, k) = (4.5, 4.5, -0.5)$

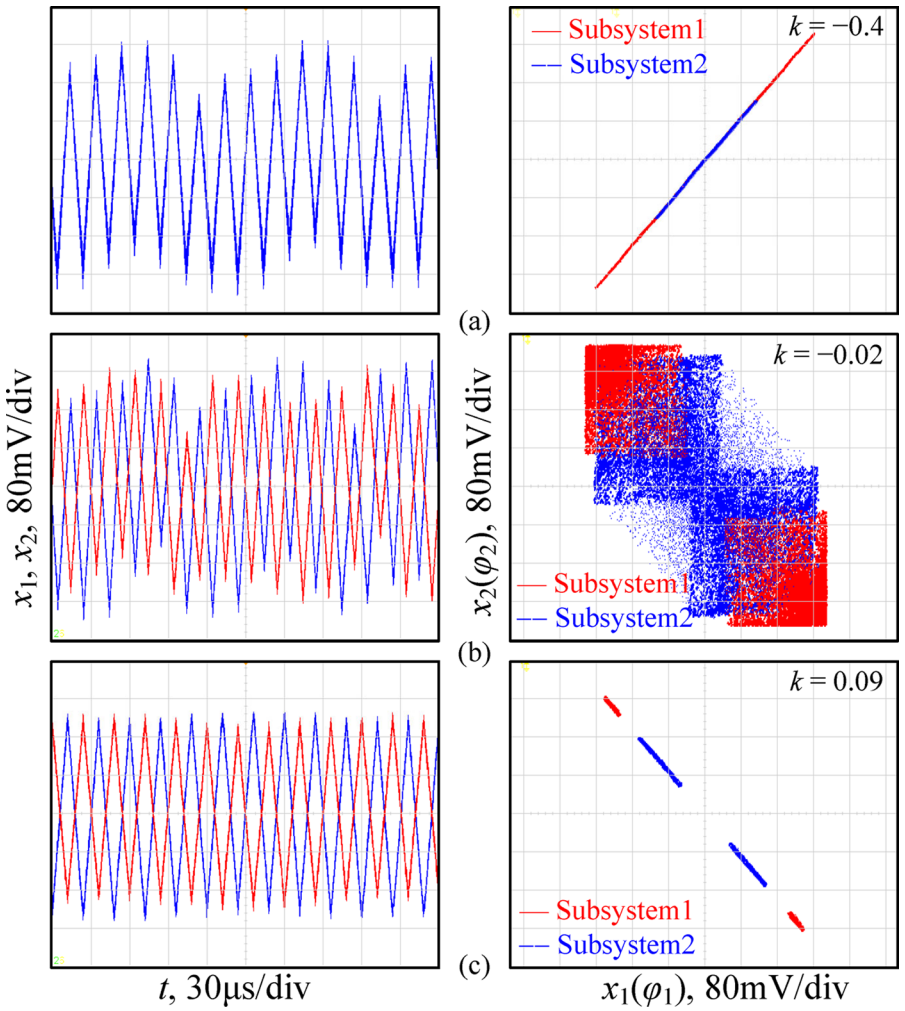

Fig. 17 The experimental synchronous behaviors for different values of coupling intensity. **a** Complete synchronization with $k = -0.4$. **b** Phase synchronization with $k = -0.02$. **c** Inverse synchronization with $k = 0.09$

coupler. Since the stability of the spatial fixed points is highly associated with the initial states of the two memristors in subsystems and the coupled memristor, it implies that extreme multistability emerges in MCMM, which is specifically expressed as the symmetric coexisting attractors and dynamical distributions. When suitable coupling intensity and initial states are selected, it is proved that MCMM realized the state transitions between complete, reverse and phase synchronizations through NMSE curves, time

sequence diagrams, and phase diagrams. In addition, different types of phase synchronization such as partial finite-time and incomplete phase synchronization were discussed by phase difference errors. It demonstrated that MCMM can regulate the initials-dependent dynamical and synchronous behaviors. What's more, the FPGA hardware platform was built to implement MCMM. Certainly, alternative discrete memristive maps and couplers can be employed to establish bidirectional coupling networks for investigating nonlinear phenomena and mechanisms of information exchange.

Author contributions Q. Zhao: Writing—original draft, Methodology, Formal analysis. H. Bao: Writing—review and editing, Validation, Investigation. X. Zhang: Formal analysis, Writing—review and editing. H. Wu: Formal analysis, Writing—review and editing. B. Bao: Supervision, Project administration, Writing—review and editing.

Funding This work was supported by the grants from the National Natural Science Foundations of China under 62271088, and 62201094, and the Postgraduate Research and Practice Innovation Program of Jiangsu Province of China under Grant No. KYCX23_3179.

Data availability Data will be made available on request.

Declarations

Conflict of interest The authors declare that they have no known competing financial interests or personal relationships that could have appeared to influence the work reported in this paper.

References

1. Díaz-Muñoz, J.D., Martínez-Fuentes, O., Cruz-Vega, I.: Predefined-time control design for tracking chaotic trajectories around a contour with an UAV. Expert Syst. Appl. **250**, 123852 (2024)
2. Man, Z., Gao, C., Dai, Y., Meng, X.: Dynamic rotation medical image encryption scheme based on improved Lorenz chaos. Nonlinear Dyn. **112**(15), 13571–13597 (2024)
3. Gu, Y., Bao, H., Yu, X., Hua, Z., Bao, B., Xu, Q.: Hybrid tri-memristor hyperchaotic map and application in Wasserstein Generative Adversarial Nets. Sci. China Technol. Sci. **67**(6), 1855–1865 (2024)
4. Panwar, A., Biban, G., Chugh, R., Tassaddiq, A., Alharbi, R.: An efficient image encryption model based on 6D hyperchaotic system and symmetric matrix for color and gray images. Heliyon **10**(11), e31618 (2024)
5. Chepuri, R., Amzalag, D., Antonsen, T.M., Girvan, M.: Hybridizing traditional and next-generation reservoir computing to accurately and efficiently forecast dynamical systems. Chaos **34**(6), 063114 (2024)
6. Gao, S., Iu, H.H.C., Wang, M., Jiang, D., El-Latif, A.A.A., Wu, R., Tang, X.: Design, hardware implementation, and application in video encryption of the 2-D memristive Cubic map. IEEE Internet Things J. **11**(12), 21807–21815 (2024)
7. Tang, J., Zhang, Z., Huang, T.: Two-dimensional cosine-sine interleaved chaotic system for secure communication. IEEE Trans. Circuits Syst. II Exp. Briefs **71**(4), 2479–2483 (2024)
8. Bao, H., Su, Y., Hua, Z., Chen, M., Xu, Q., Bao, B.: Grid homogeneous coexisting hyperchaos and hardware encryption for 2-D HNN-like map. IEEE Trans. Circuits Syst. I Regul. Pap. **71**(9), 4145–4155 (2024)
9. Tan, S., Sun, J., Tang, Y., Sun, Y., Wang, C.: Hyperchaotic bilateral random low-rank approximation random sequence generation method and its application on compressive ghost imaging. Nonlinear Dyn. **112**(7), 5037–5052 (2024)
10. Wang, M., Ding, J., Li, J., He, S., Zhang, X., Iu, H.H.C., Li, Z.: A novel multistable chaotic system with 2m-scroll attractor and its application. Eur. Phys. J. Plus **139**(1), 64 (2024)
11. Ahmadi, A., Parthasarathy, S., Pal, N., Rajagopal, K., Jafari, S., Tlelo-Cuautle, E.: Extreme multistability and extreme events in a novel chaotic circuit with hidden attractors. Int. J. Bifurcat. Chaos **33**(07), 2330016 (2023)
12. Gu, H., Li, C., Li, Y., Ge, X., Lei, T.: Various patterns of coexisting attractors in a hyperchaotic map. Nonlinear Dyn. **111**(8), 7807–7818 (2023)
13. Seetala, K.S., Clower, W., Hartmann, M., Zivanovic, S.: Physical implementation of cobalt ferrite memristor in Chua's circuit for chaotic encryption. Microelectron. Eng. **290**, 112194 (2024)
14. Han, Z., Sun, B., Banerjee, S., Mou, J.: Biological neuron modeling based on bifunctional memristor and its application in secure communication. Chaos Solitons Fractals **184**, 115020 (2024)
15. Zhao, Y., Jiang, W., Li, Y., Meng, R., Liu, M.: Analysis and test of influence of memristor non-ideal characteristics on facial expression recognition accuracy. Expert Syst. Appl. **234**, 121028 (2023)
16. Nowshin, F., Huang, Y., Sarkar, M.R., Xia, Q., Yi, Y.: Merrc: A memristor-enabled reconfigurable low-power reservoir computing architecture at the edge. IEEE Trans. Circuits Syst. I Regul. Pap. **71**(1), 174–186 (2023)
17. Eftekhari, L., Amirian, M.M.: Stability analysis of fractional order memristor synapse-coupled hopfield neural network with ring structure. Cogn. Neurodyn. **17**(4), 1045–1059 (2023)
18. Chen, C., Min, F., Cai, J., Bao, H.: Memristor synapse-driven simplified Hopfield Neural Network: hidden dynamics, attractor control, and circuit implementation. IEEE Trans. Circuits Syst. I Regul. Pap. **71**(5), 2308–2319 (2024)
19. Mou, J., Han, Z., Cao, Y., Banerjee, S.: Discrete second-order memristor and its application to chaotic map. IEEE Trans. Circuits Syst. II. Exp. Briefs **71**(5), 2824–2828 (2024)

20. Yang, F., Ma, J., Wu, F.: Review on memristor application in neural circuit and network. Chaos Solitons Fractals **187**, 115361 (2024)
21. Guo, Y., Ma, J., Zhang, X., Hu, X.: Memristive oscillator to memristive map, energy characteristic. Sci. China Technol. Sc. **67**(5), 1567–1578 (2024)
22. Li, Y., Li, C., Zhong, Q., Lei, T., Liu, S.: Attractor merging and amplitude control of hyperchaos in a self-reproducing memristive map. Int. J. Bifurcation Chaos **34**(04), 2450050 (2024)
23. Zhang, S., Li, Y., Lu, D., Wang, X., Zeng, Z.: A universal discrete memristor with application to multi-attractor generation. IEEE Trans. Circuits Syst. I Regul. Pap. (2024). https://doi.org/10.1142/S0218127424500500
24. Bao, B., Chen, L., Bao, H., Chen, M., Xu, Q.: Bifurcations to bursting oscillations in memristor-based FitzHugh-Nagumo circuit. Chaos Solitons Fractals **181**, 114608 (2024)
25. Han, J., Cheng, X., Xie, G., Sun, J., Liu, G., Zhang, Z.: Memristor-based neural network circuit of associative memory with occasion setting. IEEE Trans. Cogn. Dev. Syst. **16**(3), 1016–1026 (2024)
26. Zhang, S., Zhang, H., Lin, H., Wang, C.: Energy-based initials-boosted firings in memristor synapse-coupled bi-mRulkov neuron network. Nonlinear Dyn. **112**(14), 12411–12433 (2024)
27. Bao, H., Chen, Z., Ma, J., Xu, Q., Bao, B.: Planar homogeneous coexisting hyperchaos in bimemristor cyclic Hopfield neural network. IEEE Trans. Ind. Electron. (2024). https://doi.org/10.1109/TIE.2024.3387058
28. Yu, X., Abu Bakar, A., Li, K., Wang, Q., Sang, H.: Dynamical analysis of a novel memristor-type chaotic map. Phys. Scr. **99**(7), 075218 (2024)
29. He, S., Liu, J., Wang, H., Sun, K.: A discrete memristive neural network and its application for character recognition. Neurocomputing **523**, 1–8 (2023)
30. Chen, B., Liu, F., Iu, H.H.C., Bao, H., Xu, Q.: Memristive neural network circuit of operant conditioning with reward delay and variable punishment intensity. IEEE Trans. Circuits Syst. II Exp. Briefs **71**(3), 1002–1006 (2024)
31. Xu, Q., Fang, Y., Feng, C., Parastesh, F., Chen, M., Wang, N.: Firing activity in an N-type locally active memristor-based Hodgkin-Huxley circuit. Nonlinear Dyn. **112**(15), 13451–13464 (2024)
32. Wang, C., Liang, J., Deng, Q.: Dynamics of heterogeneous Hopfield neural network with adaptive activation function based on memristor. Neural Netw. **178**, 106408 (2024)
33. Tamba, V.K., Biamou, A.L.M., Tagne, F.K., Takougang, C.A.N., Fotsin, H.: Hidden extreme multistability in a smooth flux-controlled memristor based four-dimensional chaotic system and its application in image encryption. Phys. Scr. **99**(2), 025210 (2024)
34. Xie, Y., Wang, X., Li, X., Ye, Z., Wu, Y., Yu, D., Jia, Y.: Energy consumption in the synchronization of neurons coupled by electrical or memristive synapse. Chin. J. Phys. **90**, 64–82 (2024)
35. Huang, H., Xu, J., Wang, J., Chen, X.: Reinforcement learning-based secure synchronization for two-time-scale complex dynamical networks with malicious attacks. Appl. Math. Comput. **479**, 128840 (2024)
36. Baluni, S., Yadav, V., Das, S.: Quasi-projective synchronization of non-identical time-varying delayed quaternion-valued neural networks with interaction terms: direct method. Eng. Appl. Artif. Intell. **136**, 108866 (2024)
37. Guo, Y., Xie, Y., Wang, C., Ma, J.: Energy and synchronization between two neurons with nonlinear coupling. Cogn. Neurodyn. **18**, 1835–1847 (2024)
38. Eshaghi, S., Kadkhoda, N.: Inc: Chaos control and synchronization of a new fractional laser chaotic system. Qual. Thero. Dyn. Syst. **23**(5), 241 (2024)
39. Xie, Y., Xu, Y., Ma, J.: Desynchronization and energy diversity between neurons. Nonlinear Dyn. **111**(12), 11521–11541 (2023)
40. Chu, Y., Li, X., Han, X.: Exponential synchronization of complex networks with unmeasured coupling delays via impulsive observer and impulsive control. Appl. Math. Comput. **479**, 128843 (2024)
41. Xu, Q., Liu, T., Ding, S., Bao, H., Li, Z., Chen, B.: Extreme multistability and phase synchronization in a heterogeneous bi-neuron Rulkov network with memristive electromagnetic induction. Cogn. Neurodyn. **17**(3), 755–766 (2023)
42. Vijay, S.D., Thamilmaran, K., Ahamed, A.I.: Transition to extreme events in a coupled memristive Hindmarsh-Rose neuron system. Eur. Phys. J. Plus **139**(3), 1–10 (2024)
43. Chen, M., Luo, X., Suo, Y., Xu, Q., Wu, H.: Hidden extreme multistability and synchronicity of memristor-coupled non-autonomous memristive Fitzhugh-Nagumo models. Nonlinear Dyn. **111**(8), 7773–7788 (2023)
44. Namura, N., Nakao, H.: Optimal coupling functions for fast and global synchronization of weakly coupled limit-cycle oscillators. Chaos Solitons Fractals **185**, 115080 (2024)
45. Zhang, S., Zhang, H., Lin, H., Wang, C.: Energy-based initials-boosted firings in memristor synapse-coupled bi-mRulkov neuron network. Nonlinear Dyn. **112**(12), 12411–12433 (2024)
46. Hu, J., Bao, H., Xu, Q., Chen, M., Bao, B.: Synchronization generations and transitions in two map-based neurons coupled with locally active memristor. Chaos Solitons Fractals **184**, 114993 (2024)
47. Peng, L., Bi, D., Li, X., Li, H., Tang, Y., Xie, Y.: Multi-synchronization of coupled multi-stable memristive Cohen-Grossberg neural networks with mixed time-delays. Expert Syst. Appl. **255**, 124501 (2024)
48. Bao, H., Rong, K., Chen, M., Zhang, X., Bao, B.: Multistability and synchronization of discrete maps via memristive coupling. Chaos Solitons Fractals **174**, 113844 (2023)
49. Li, Y., Wang, M., Chang, H., Wang, H., Chen, G.: A hyperchaotic memristive system with extreme multistability and conservativeness. Nonlinear Dyn. **112**(5), 3851–3868 (2024)
50. Chen, M., Luo, X., Zhang, Y., Wu, H., Xu, Q., Bao, B.: Initial-boosted behaviors and synchronization of memristor-coupled memristive systems. EEE Trans. Circuits Syst. I. Regul. Pap. **71**(2), 781–793 (2023)
51. Bao, B., Zhao, Q., Yu, X., Wu, H., Xu, Q.: Complex dynamics and initial state effects in a two-dimensional sine-bounded memristive map. Chaos Solitons Fractals **173**, 113748 (2023)
52. Li, K., Bao, B., Ma, J., Chen, M., Bao, H.: Synchronization transitions in a discrete memristor-coupled bi-neuron model. Chaos Solitons Fractals **165**(2), 112861 (2022)
53. Li, Y., Li, C., Zhong, Q., Liu, S., Lei, T.: A memristive chaotic map with only one bifurcation parameter. Nonlinear Dyn. **112**(5), 3869–3886 (2024)

54. Li, J., Wang, C., Deng, Q.: Symmetric multi-double-scroll attractors in Hopfield neural network under pulse controlled memristor. Nonlinear Dyn. **112**(16), 14463–14477 (2024)
55. Gao, Z., Liu, L., Wang, Y., Gao, P., Li, Y.: Stabilization and synchronization control for complex dynamical networks with dynamic link subsystem. Inf. Sci. **609**, 1588–1600 (2022)
56. Chen, M., Xue, W., Luo, X., Zhang, Y., Wu, H.: Effects of coupling memristors on synchronization of two identical memristive Chua's systems. Chaos Solitons Fractals **174**, 113780 (2023)